Vortex-Wide Detection of Large Aspherical NAT Particles in the Arctic Winter 2011/12 Stratosphere

W. Woiwode[1] [iD], **M. Höpfner**[1] [iD], **L. Bi**[2] [iD], **F. Khosrawi**[1], and **M. L. Santee**[3] [iD]

[1]Institute of Meteorology and Climate Research–Atmospheric Trace Gases and Remote Sensing (IMK-ASF), Karlsruhe Institute of Technology, Karlsruhe, Germany, [2]School of Earth Sciences, Zhejiang University, Hangzhou, China, [3]Jet Propulsion Laboratory, California Institute of Technology, Pasadena, California, USA

Abstract Micron-sized HNO_3-containing particles in polar stratospheric clouds are known to denitrify the polar winter stratosphere and support chemical ozone loss. We show that populations of nitric acid trihydrate (NAT) particles with volume-equivalent median radii of 3–7 μm can be detected vortex-wide by means of infrared limb sounding. Key for detection are the applied optical characteristics of highly aspherical particles consisting of the β-NAT phase. Spectroscopic signatures and ambient conditions of detected populations show that these particles play a key role in denitrification of the Arctic winter stratosphere. Complementary gas-phase HNO_3 observations indicate collocated highly efficient HNO_3 sequestration within days and are consistent with measured spectral signals of populations of large NAT particles. High amounts of condensed gas-phase equivalent HNO_3 exceeding 10 ppbv and long persistence of detected populations, despite expected gravitational settling, imply that our understanding of the particles is incomplete.

Plain Language Summary In the past, micron-sized HNO_3-containing particles characterized by significant gravitational settling and denitrifying the polar stratosphere were postulated to explain observed HNO_3-distributions in the polar stratosphere. The long-sought large nitric acid trihydrate particles were observed for the first time about 20 years ago. However, important aspects of these particles remained unclear. A decade later, field observations of these particles were found to be not compatible with established model simulations and question our understanding of polar stratospheric chemistry.

Here, we present a new method to detect such populations of HNO_3-containing particles by using infrared limb observations. Our study contributes redundant spectral and thermodynamic evidence for the particle composition and furthermore indications of particle shape. Based on complementary observations, we track populations of large nitric acid trihydrate particles during the Arctic winter 2011/12. We find rapid particle growth, highly efficient sequestration of gas-phase HNO_3, and at the same time unexpectedly long persistence times of the observed populations. All of these aspects are not captured by state-of-the-art model simulations reported in the literature. Thus, our method provides the prerequisite to test and optimize model simulations of these particles during entire winters, with the goal to improve future projections of polar stratospheric ozone.

1. Introduction

Large HNO_3-containing particles in polar stratospheric clouds (PSCs) sediment and denitrify the polar winter stratosphere and thus support chemical ozone loss (Fahey et al., 1990; Peter, 1997; Poole & McCormick, 1988; Salawitch et al., 1989; Solomon, 1999; Toon et al., 1986; Waibel et al., 1999). The particles are thought to be composed predominantly of solid nitric acid trihydrate (NAT) and have radii between 5 and 10 μm (Fahey et al., 2001; Hanson & Mauersberger, 1988). While extensive denitrification is common in the cold Antarctic winter stratosphere, the Arctic winter stratosphere is mostly warmer, and extensive denitrification is linked to individual cold winters (Fahey et al., 1990; Toon et al., 1990). In context of climate and atmospheric composition change, a high year-to-year variability and a trend to colder stratospheric temperatures were diagnosed in the Arctic (Rex et al., 2006; Rieder & Polvani, 2013; WMO (World Meteorological Organization), 2018). Extensive denitrification and ozone loss were clearly observed in recent extreme Arctic winters (Khosrawi et al., 2011; Khosrawi et al., 2017; Kuttippurath et al., 2012; Manney et al., 2011; Sinnhuber et al., 2011). Accurate representations of Arctic winter denitrification and chemical ozone loss are

essential for future projections of stratospheric ozone (WMO (World Meteorological Organization), 2018). Among other factors, significant uncertainties remain due to limited knowledge of the characteristics of large NAT particles (Grooß et al., 2014; Tritscher et al., 2019; Zhu et al., 2015).

NAT is stable at temperatures below ~195 K (Hanson & Mauersberger, 1988; Tizek et al., 2004; Worsnop et al., 1993) and was confirmed by in situ observations in the Arctic stratosphere (Voigt et al., 2000). Further constituents of PSCs are supercooled ternary solutions (STS) and ice (Peter, 1997). Large HNO_3-containing particles denitrifying the Arctic winter stratosphere were detected in situ and attributed to NAT (Brooks et al., 2003; Fahey et al., 2001; Northway et al., 2002). Lidar remote sensing observations allow detection of NAT-containing PSCs operationally (Achtert & Tesche, 2014; Pitts et al., 2018) but are hardly sensitive to particle sizes. A characteristic spectral peak in space-borne infrared limb observations was clearly assigned to the v_2 out-of-plane deformation band of NO_3- in β-NAT, and a detection method sensitive to small NAT particles in high volume densities, which occur for example in lee-wave events, was established (Höpfner et al., 2006; Spang & Remedios, 2003). Laboratory experiments suggest that β-NAT particles are highly aspherical (Grothe et al., 2006). In a case study involving airborne in situ and infrared limb observations, large highly aspherical β-NAT particles with equivalent radii exceeding 10 μm were detected (Molleker et al., 2014; Woiwode et al., 2016). Compared to previous observations, a high gas-phase equivalent HNO_3 mixing ratio of 9 ppbv was inferred from the airborne limb observations, while the in situ observations supported even higher values. State-of-the art model parameterizations were not able to reproduce the observed combinations of large particle sizes and high HNO_3 content inferred from these case studies (Grooß et al., 2014; Zhu et al., 2015).

In the past, irreversible denitrification of the Arctic winter stratosphere was successfully simulated using a microphysical model of large NAT particles (Carslaw et al., 2002). Similar and advanced parameterizations (Engel et al., 2013; Hoyle et al., 2013; Zhu et al., 2015) were applied to simulate denitrification in subsequent and, particularly, colder Arctic and Antarctic winters (Grooß et al., 2005; Grooß et al., 2014; Zhu et al., 2015; Khosrawi et al., 2017; Zhu et al., 2017; Zhu et al., 2017; Tritscher et al., 2019). However, nucleation, growth, and sedimentation characteristics of large NAT particles remain largely uncertain. Ice is likely to play an important role in NAT nucleation (Weiss et al., 2016). While state-of-the-art parameterizations of large NAT particles are successful in reproducing major patterns of denitrification and the state at the end of the winter, large discrepancies remain in direct comparisons with rare Arctic particle field observations (Grooß et al., 2014; Molleker et al., 2014; Woiwode et al., 2016; Zhu et al., 2015). Depending on the different models and scenarios, simulated particle sizes are significantly smaller and/or number densities significantly lower than observed. Condensed HNO_3 inferred from the observations is underestimated by up to one order of magnitude. Moreover, relying on the common approximation of spherical particles, field observations of extremely large NAT particles would imply a much faster sedimentation and more efficient irreversible denitrification than simulated. As a consequence, uncertainties remain in simulations and projections of polar stratospheric reactive nitrogen (NO_y) and ultimately chemical ozone loss. Clearly, vortex-wide observational capabilities sensitive to large NAT particles that allow model parameterizations to be tested are lacking.

2. Methods

2.1. New Method to Detect Large NAT Particles

Here, we introduce a new method for vortex-wide and specific detection of aspherical β-NAT particle populations with median radii of 3–7 μm. The method is based on radiative transfer calculations of infrared limb observations (Stiller et al., 2002) accounting for the light scattering by micron-sized particles (Höpfner et al., 2006). We apply our method to space-borne observations by the Michelson Interferometer for Passive Atmospheric Sounding (MIPAS) (Fischer et al., 2008). Particle size distributions are implemented by means of lognormal distributions and are characterized by median radius r, mode width σ, and number density N. Simulations of spectra of spherical β-NAT particles, STS droplets, and spherical ice particles are based on Mie calculations (Höpfner et al., 2006). Simulations of highly aspherical β-NAT particles are based on T-Matrix calculations (Bi et al., 2013) and are used to define the criteria of our method. As in Woiwode et al. (2016), we adopt elongated spheroids with an aspect ratio of 0.1. Note that highly oblate spheroids with an aspect ratio of 10 produced similar results in the previous study. Refractive indices of β-NAT, STS, and ice
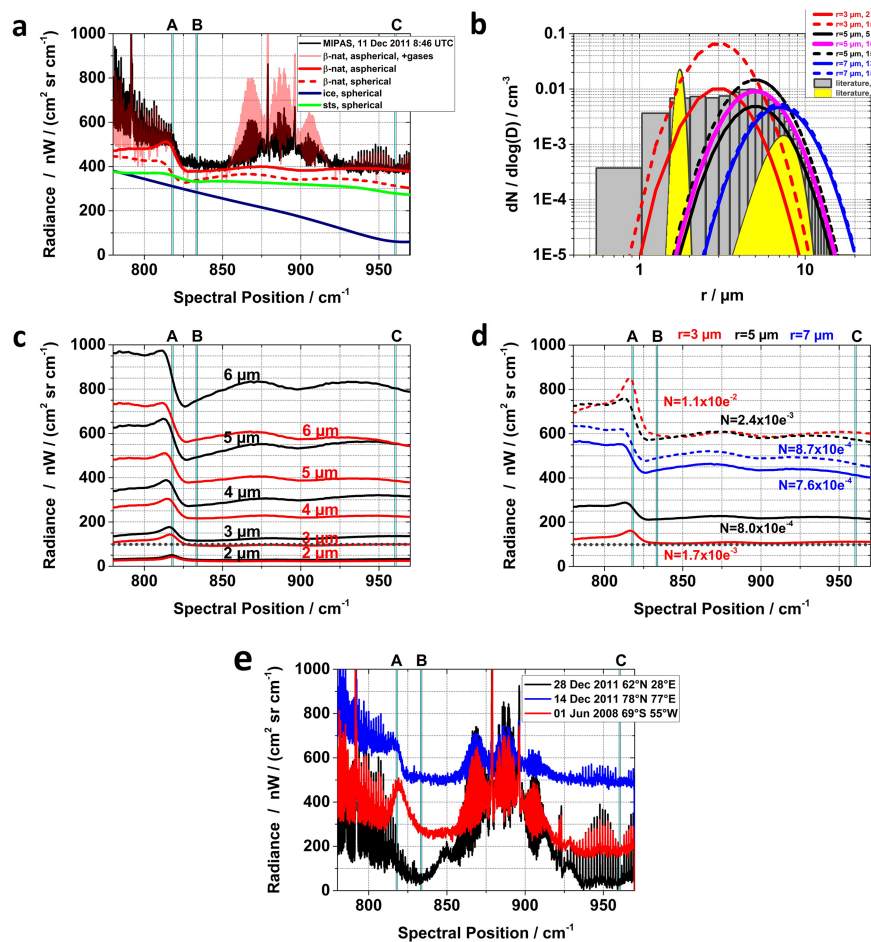
Figure 1. Observed and simulated signatures of β-NAT populations. (a) Spectrum as observed by MIPAS at a tangent altitude of 18.7 km (black line). Simulations of aspherical β-NAT particles including and excluding trace gases (red transparent and solid lines), spherical β-NAT particles (red dashed line), STS (solid green line), and ice (solid dark blue line). (b) Size distributions from the literature for the same day (gray, from Woiwode et al., 2016 and based on Molleker et al., 2014) and used for simulations in (a), from the literature for the winter 1999/2000 (yellow, from Fahey et al., 2001), and used for sensitivity simulations (red, pink, black and blue solid/dashed lines) in (c,d). (c) Sensitivity simulations of spectra of aspherical β-NAT particles using size distributions with different r (indicated), excluding and including effects by high tropospheric clouds (black and red solid lines, respectively). (d) Range of detection, determined from simulations including effects by a high tropospheric cloud and using different combinations of r and N (red, black, and blue, corresponding with Panel b). (e) MIPAS observations of a cloud-free case (black), a developed β-NAT "peak" ($r \leq 3$ μm, high volume density, red) and a developed "shoulder" of aspherical β-NAT particles ($r \geq 3$ μm, high amounts of condensed HNO_3, blue). Microwindows used to detect aspherical NAT populations with $r \geq 3$ μm are marked in cyan in (a,c,d, and e). Gray dotted horizontal lines in (c,d) indicate the overall threshold radiance level of our method.

reported in the literature are used (Biermann, 1998; Biermann et al., 2000; Zasetsky et al., 2005; Höpfner et al., 2006).

Figure 1a shows a typical MIPAS spectrum which exhibits the characteristic spectral signature of large aspherical β-NAT particles: a "shoulder-like" signature around 820 cm^{-1} and an overall high and flat spectral baseline. Geolocation and time of the observation approximately coincide with airborne observations reported in the literature (compare (Molleker et al., 2014; Woiwode et al., 2016)). Also shown are two simulations of aspherical β-NAT particles (including and excluding climatological trace gas profiles), spherical β-NAT particles, STS droplets, and ice particles. The same size distribution constrained by the previous airborne case study is used (gray in Figure 1b; see Woiwode et al., 2016 and based on Molleker et al., 2014). Other than small discrepancies (discussed below), the spectral baselines of both simulated spectra of aspherical β-NAT particles and the observation agree well, particularly in the narrow spectral windows

"A", "B", and "C" (cyan) which are used in our method. The simulation of spherical β-NAT particles does not adequately reproduce the signature around 820 cm^{-1} and shows an underlying negative gradient (i.e., "tilt" of the spectral baseline with increasing wave numbers to lower radiances). The STS simulation shows hardly any modulation around 820 cm^{-1} and also has an overall negative gradient, and the ice simulation exhibits a steep negative gradient and lacks any specific signatures. Thus, the signature of large aspherical β-NAT particles can be clearly distinguished from STS and ice.

The simulations of aspherical β-NAT particles also show some noticeable discrepancies from the observations. Discrepancies between 850 and 925 cm^{-1} are explained by the fact that the climatological gas-phase HNO$_3$ profile used in the simulation does not represent the actual state of denitrification. Therefore, the gas-phase HNO$_3$ spectral lines are overestimated. In contrast, stratospheric CO$_2$ mixing ratios are well-known, and corresponding spectral lines above 925 cm^{-1} are reproduced well. Furthermore, the observation shows a negative baseline gradient below 850 cm^{-1}. This discrepancy between observation and simulation is explained by altitude-dependent variations of the β-NAT size distribution, weak contributions by potential ice particles present at higher altitudes (i.e., inducing an underlying negative gradient), and uncertainties in the simulated dense ozone lines based on a climatological ozone profile. However, these discrepancies hardly affect our method which is based on the microwindows A, B, and C.

The following integrated radiances and their differences are used to detect the flat "hockey stick" signature of large aspherical β-NAT particles from 817.5 to 961 cm^{-1}. (i) An integrated radiance of ≥100 nW cm^{-2} sr^{-1} in the spectral window "C" (960.0 to 961.0 cm^{-1}). (ii) A difference between the integrated radiances in the spectral windows "B" (833.0 to 834.0 cm^{-1}) and "C" of ≤100 nW cm^{-2} sr^{-1}. (iii) A difference between the integrated radiances in "A" (817.5 to 818.5 cm^{-1}) and "B" of ≥50 nW cm^{-2} sr^{-1}. More information on PSC detection methods used here is provided in the supplement.

2.2. Sensitivity

To test the sensitivity of our method, modified simulations are shown in Figures 1c and 1d. Our baseline case involves a size distribution with $r = 5$ μm, $σ = 1.35$, and $N = 1.5 \cdot 10^{-3}$ cm^{-3} (pink solid line in Figure 1b). The spectrum of large β-NAT particles is modulated by the radius and greybody-like radiation originating from the ground or tropospheric clouds scattered by the β-NAT particles. Figure 1c shows simulations of aspherical β-NAT particles including the baseline case with modified radii from 2 to 6 μm. Note that except for the size distribution adapted from the previous study for the same day (grey), unbinned size distributions are shown in Figure 1b for easier reading. The size distributions used in Figure 1c correspond to gas-phase equivalent HNO$_3$ mixing ratios of 0.6 ($r = 2$ μm), 2 ($r = 3$ μm), 5 ($r = 4$ μm), 10 ($r = 5$ μm), and 16 ppbv ($r = 6$ μm). These scenarios cover cases with low fractions of HNO$_3$ being condensed to cases with almost all HNO$_3$ being condensed (compare MLS ambient HNO$_3$ mixing ratios in Figures 2a and 2b). Note that radii of volume-equivalent spheres are given here and not diameters (compare Carslaw et al., 2002; Fahey et al., 2001; Molleker et al., 2014). Black solid lines in Figure 1c show simulations assuming no tropospheric clouds. Red solid lines show the same simulations including an optically dense tropospheric cloud top at 10 km. The simulations show that a cold tropospheric cloud top induces a weaker overall signal and modulates the spectrum. However, the criteria of our method are fulfilled in the cases with median radii equal to or larger than 3 μm. Only the $r = 3$ μm scenario including a cold tropospheric cloud top shown here falls slightly below the detection threshold.

The spectrum sensitivity to different particle number densities is investigated in Figure 1d for $r = 3$, 5, and 7 μm. The solid red, black, and blue lines correspond to cases which are just detectable under the attenuating conditions of high tropospheric clouds, which are often found in Arctic winters. Here, the NAT "shoulder" at 820 cm^{-1} is developed sufficiently (see criterion (iii)). The scenarios correspond to 2 ($r = 3$ μm), 5 ($r = 5$ μm), and 13 ppbv ($r = 7$ μm) of gas-phase equivalent HNO$_3$. The loss in sensitivity with increasing median radius is a consequence of the increasing size parameter (see Bi et al., 2013 and references therein) and flattening of the signature at 820 cm^{-1}. The dashed lines are cases with 15 ppbv of gas-phase equivalent HNO$_3$, approximating situations with complete condensation of all available HNO$_3$. Associated number densities are also indicated in Figure 1d, and the corresponding size distributions are shown in Figure 1b using the same color scheme. Note that the signature around 820 cm^{-1} shows a partially peak-like shape for $r = 3$ μm (cf. Höpfner et al., 2006). So in summary, within the assumptions made in our sensitivity scenarios, our method based on
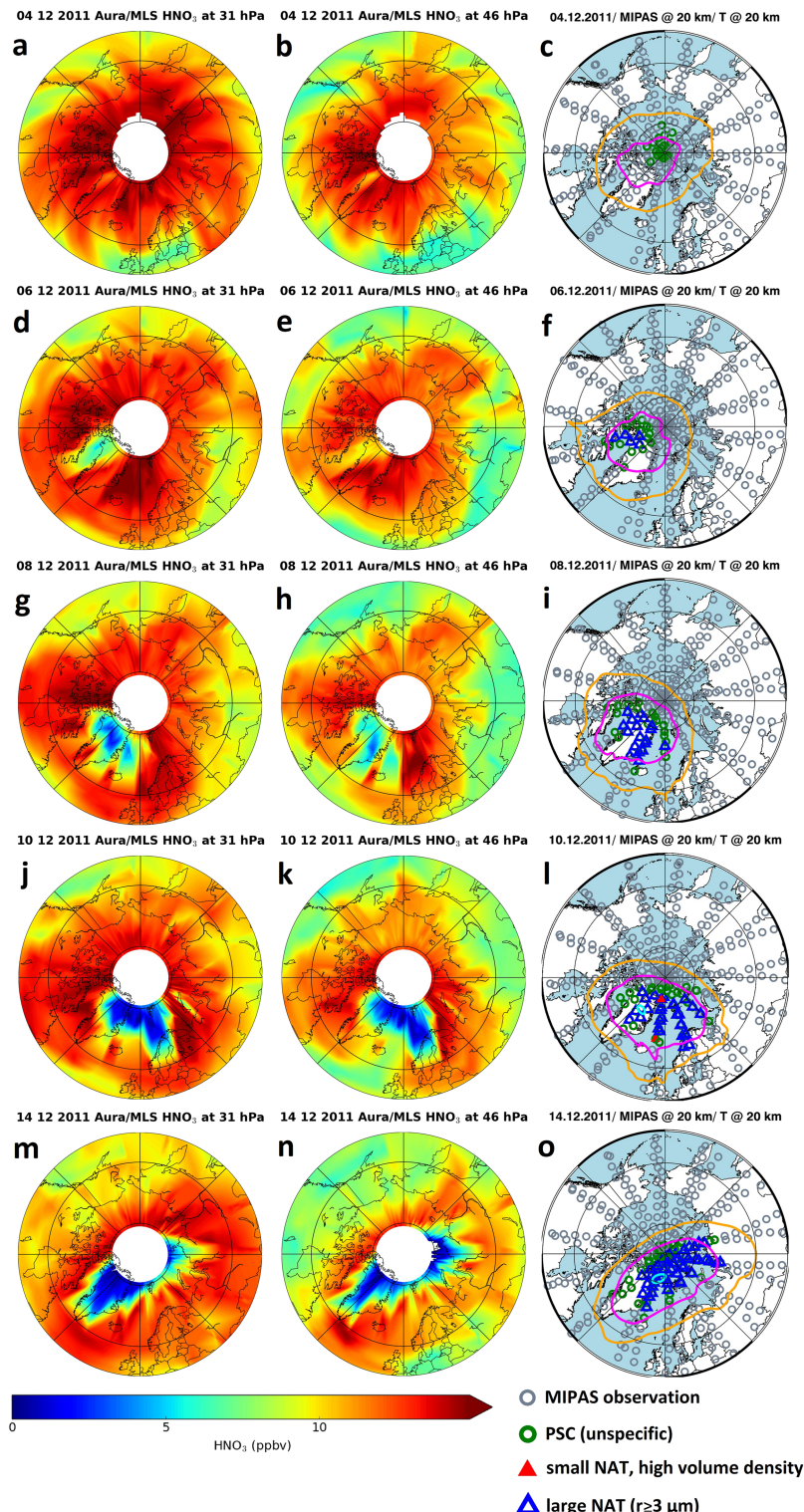
Figure 2. Onset of Arctic winter 2011/12 denitrification and detection of NAT particles with volume-equivalent radii ≥ 3 μm. (a–o) MLS gas-phase HNO_3 observations (colored contours) at approximately 22 (left column) and 20 km (middle column). MIPAS observations (right column) at 20 km (open gray circles), PSCs detected using the cloud index method (open green circles), populations of small NAT particles in high volume densities (filled red triangles), and populations of large aspherical NAT particles (open blue triangles). ECMWF temperature isolines are shown at 200 (orange), 195 ($\sim T_{NAT}$, magenta), and 190 K (~ 2 K above T_{ice}, cyan). The inner and outer black solid circles in the panels mark latitudes of 60°N and 80°N.

integrated radiances and their differences is capable of detecting NAT particle populations with equivalent median radii of 3–7 μm and condensed gas-phase equivalent HNO_3 exceeding 2–13 ppbv.

In Figure 1b, the applied size distributions are compared to the size distribution reported for the Arctic winter 1999/2000 field observations (yellow, Fahey et al., 2001). All size distributions with $r \geq 3$ μm accessible to our method considerably exceed this size distribution in terms of number densities and condensed HNO_3. Furthermore, size distributions simulated in different model studies are well exceeded for the same parameters (compare, Carslaw et al., 2002; Grooß et al., 2014; Zhu et al., 2015).

Note, our method may also respond to NAT populations with $r \leq 3$ μm in high volume densities, if the integrated radiance in the spectral window "C" exceeds 100 nW cm^{-2} sr^{-1} and the slope of the spectral baseline is sufficiently low (i.e., "B"–"C" ≤ 100 nW cm^{-2} sr^{-1}). Therefore, our method should be used in combination with the established method for the detection of small NAT particles in high volume densities reported in the literature (Höpfner et al., 2006) to distinguish between large NAT particles and small NAT particles in high volume densities. MIPAS spectra of a cloud-free case and cases with developed signatures of small NAT particles in high volume densities and large NAT particles with $r \geq 3$ μm consuming high amounts of HNO_3 are shown in Figure 1e.

3. Complementary MIPAS and MLS Observations

In the following section, we apply our method sensitive to populations of aspherical β-NAT particles with median radii of 3 to 7 μm and gas-phase equivalent HNO_3 exceeding 2 to 13 ppbv to MIPAS observations during the onset of denitrification in the 2011/12 Arctic winter. The formation of such populations is associated with significant sequestration of HNO_3 from the gas phase. The space-borne microwave limb sounder (MLS) is capable of measuring gas-phase HNO_3 in the presence of PSCs (Livesey et al., 2018; Manney et al., 2015; Waters et al., 2006). We use MLS observations to test whether gas-phase HNO_3 depletion detected by MLS is consistent with populations of large NAT particles detected by MIPAS. Furthermore, we assess the extent of gas-phase HNO_3 sequestration using the MLS data and thereby constrain the maximum possible amount of HNO_3 condensed in the detected populations. Finally, we estimate condensed HNO_3 from MIPAS observations and compare with that inferred from the MLS gas-phase HNO_3 observations.

The onset of widespread PSC formation and HNO_3 sequestration is detected by MIPAS and MLS in early December 2011. The left and middle columns of Figure 2 show MLS gas-phase HNO_3 observations at the pressure (altitude) levels of 31 hPa (~22 km) and 46 hPa (~20 km). These are the altitudes where PSCs, HNO_3 sequestration, and denitrification are typically found in the Arctic (Pitts et al., 2018; Waibel et al., 1999). In the right column, we show MIPAS observations at 20 km, where NAT particles are expected to grow to large sizes during gravitational settling (Carslaw et al., 2002; Fahey et al., 2001). PSCs detected by the sensitive but unspecific cloud index method (see Spang et al., 2004), populations of small NAT particles ($r \leq 3$ μm) in high volume densities (see Höpfner et al., 2006), and populations of large aspherical NAT particles ($r \geq 3$ μm) detected by our new method are highlighted. ECMWF ERA-Interim (European Centre for Medium-Range Weather Forecasts, https://www.ecmwf.int/) temperature contours at the same altitude level provide the thermodynamic context. Temperature isolines are shown at 200 K, which is an upper limit allowing the persistence of NAT particles under enhanced HNO_3 partial pressures, and at 195 K, which is the typical value of the existence temperature of NAT (T_{NAT}) in the stratosphere (Hanson & Mauersberger, 1988). The isoline at 190 K marks lower temperatures which are still above the ice frost point (T_{ice}~188 K (Murphy & Koop, 2005)).

4. Vortex-Wide Detection in Arctic winter 2011/12

On 4 December 2011, the gas-phase HNO_3 distribution north of 60°N is largely unperturbed. At 22 and 20 km, HNO_3 mixing ratios are mostly higher than 12 and 10 ppbv, respectively (Figures 2a and 2b). Only a weak local minimum is found at 20 km above the north-west coast of Greenland. An unspecified PSC population is detected by MIPAS over the pole at temperatures around T_{NAT} (Figure 2c). Two days later, significant local gas-phase HNO_3 depletion of more than 5 ppbv (2–3 ppbv) relative to ambient HNO_3 mixing ratios is identified above north-west Greenland and Baffin Bay at 22 km (20 km), indicating efficient gas-phase HNO_3 sequestration by PSCs (Figures 2d and 2e). At the same time, the PSC population detected by
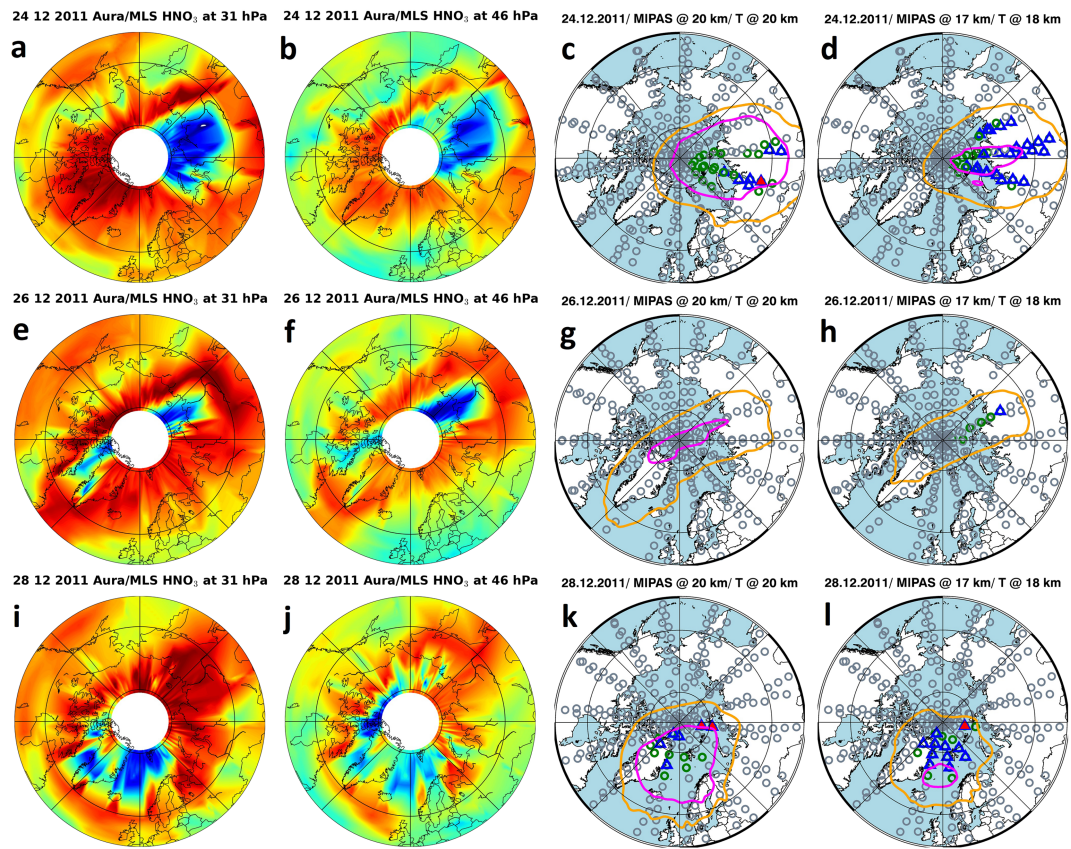
Figure 3. Strong short-term modulations in populations of NAT particles with volume-equivalent radii ≥3 μm, for legend see Figure 2. The fourth column furthermore includes MIPAS observations and ECMWF temperature contours at the levels of ~17 and ~18 km, respectively.

MIPAS has spread out in the same region, and a population of large NAT particles is detected coincident with local gas-phase HNO_3 depletion detected by MLS (Figure 2f).

On 8 and 10 December 2011, regions depleted in gas-phase HNO_3 at 22 km (Figures 2g and 2j) and 20 km (Figures 2h and 2k) spread out rapidly on synoptic scales across Greenland to Scandinavia. Local minimum gas-phase HNO_3 mixing ratios fall below 5 ppbv (2 ppbv) on 8 December 2011 (10 December 2011), which are in contrast to much higher mixing ratios of 10 to 15 ppbv in surrounding air masses. At the same time, the population of large NAT particles detected by MIPAS (Figures 2i and 2l) spreads out further in exactly the same region. Ambient temperatures remain slightly below T_{NAT} and mostly well above T_{ice}. On 10 December 2011, indications of small NAT particles in high volume densities are found locally above the Arctic sea and close to the pole (Figures 2l). On 14 December 2011, the regions depleted in gas-phase HNO_3 at 22 and 20 km have spread out further and cover wide regions from Greenland to northern Siberia (Figures 2m and 2n). Gas-phase HNO_3 mixing ratios approach zero, indicating almost complete condensation of HNO_3. The detected populations of large NAT particles follow the regions depleted in gas-phase HNO_3 consistently, whereas temperatures remain below T_{NAT} and above T_{ice} (Figure 2o).

Strong short-term modulations of populations of large NAT particles are documented in Figure 3. By 24 December 2011, after extensive gas-phase HNO_3 depletion and populations of the particles persisting over weeks (not shown), the region depleted in gas-phase HNO_3 covers a wide area in the sector from Siberia to the pole (Figures 3a and 3b). While synoptic minimum temperatures at 20 km remain below T_{NAT} and above T_{ice}, indications of NAT particles with volume-equivalent median radii ≥3 μm remain only locally above Siberia (Figure 3c). Wide areas have been irreversibly denitrified. HNO_3 removed from this level by gravitational settling of large NAT particles might be still present in the condensed phase at lower altitudes.
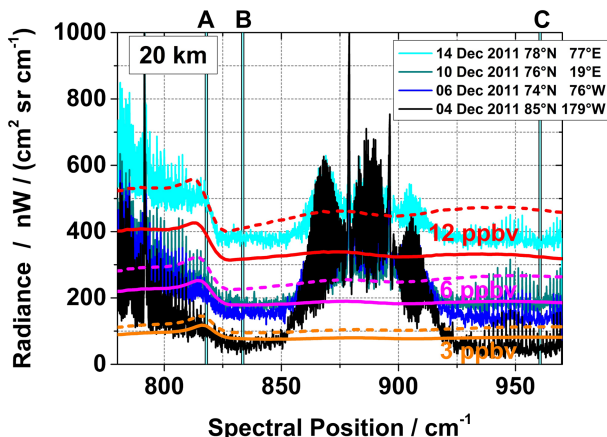
Figure 4. Observed spectra of NAT populations and estimates of condensed HNO₃. The MIPAS spectra with a tangent altitude of 20 km are associated with large NAT particle detections. Sensitivity simulations for r = 3, 4, and 5 μm (orange, magenta, and red) including and excluding effects by high tropospheric clouds (solid and dashed lines, respectively) are superimposed. Microwindows used to detect aspherical NAT populations with $r \geq 3$ μm are marked in cyan.

To test this hypothesis, we show also MIPAS observations at the level of 17 km (Figure 3d). In fact, a widespread population of large NAT particles that coincides well with the region depleted in gas-phase HNO₃ above is found at 17 km. Two days later, the denitrified area stretches across the pole to Greenland and Canada (Figures 3e and 3f). Hardly any indications of PSCs remain due to warmer temperatures (Figures 3g and 3h). However, only another 2 days later, the denitrified air masses are located mainly at a region around Greenland and the Arctic sea (Figures 3i and 3j), and a PSC including populations of large NAT particles has been reestablished in the same region (Figures 3k and 3l). Note that such populations are located preferentially in regions where enhanced supersaturation of gas-phase HNO₃ versus the NAT phase is found locally, which is consistent with the thermodynamic characteristics of NAT (Hanson & Mauersberger, 1988).

Examples of MIPAS spectra of NAT populations detected by our method are shown in Figure 4 together with reference simulations (see Figure 1 c). For the reference simulations, the corresponding gas-phase equivalent HNO₃ mixing ratio at 20 km is indicated for comparisons with the MLS data (see Figure 2, middle column). On 4 December 2011, before the beginning of significant HNO₃ sequestration, the shown MIPAS spectrum corresponds to less than 3 ppbv of condensed gas-phase equivalent HNO₃. The spectrum of 6 December 2011 corresponds to more than 3 ppbv and the spectrum of 10 December 2011 to up to 6 ppbv of condensed gas-phase equivalent HNO₃. The spectrum of 14 December 2011 corresponds to a rather high amount of condensed HNO₃ of about 12 ppbv. All gas-phase equivalent HNO₃ mixing ratios estimated from the MIPAS spectra are in keeping with HNO₃ depletion seen in the complementary MLS data.

5. Conclusions

The MLS and MIPAS observations in the Arctic winter 2011/12 clearly show fast and extensive sequestration of gas-phase HNO₃ within only a few days and coincident formation of widespread populations of large aspherical NAT particles. The observations are consistent with established spectral (Biermann, 1998; Höpfner et al., 2006) and thermodynamic (Hanson & Mauersberger, 1988; Tizek et al., 2004; Worsnop et al., 1993) characteristics of β-NAT and show that large aspherical β-NAT particles play a key role in denitrification of the Arctic winter stratosphere. Extensive gas-phase HNO₃ sequestration measured by MLS and condensed HNO₃ inferred from the MIPAS spectra of 10 ppbv or more exceed model simulations for different Arctic winters by up to one order of magnitude (Carslaw et al., 2002; Fahey et al., 2001; Grooß et al., 2014; Zhu et al., 2015). NAT particles with radii around 5 μm are expected to sediment with fall speeds of about one kilometer per day (Fahey et al., 2001), which would result in the removal of particles of the sizes observed here after only a few days. In contrast, we find populations of large NAT particles at 20 km persisting over more than 1 week. The long persistence and slow sedimentation of the detected populations could be explained by rather low fall speeds of highly aspherical particles (Westbrook, 2008). Further focused field observations would be extremely helpful to constrain the microphysical properties of large NAT particles. Model parameterizations should be revisited in order to reproduce observations of large NAT particles to improve future projections of polar stratospheric ozone.

Data Availability Statement

The MIPAS observations used here are accessible via https://earth.esa.int/web/guest/pi-community/apply-for-data/fast-registration. The MLS data used here are available at https://disc.gsfc.nasa.gov/datasets/ML2HNO3_V004/summary. The ECMWF ERA-Interim data used here are accessible at https://www.ecmwf.int/en/forecasts/datasets/reanalysis-datasets/era-interim.

Conflicts of Interest

The authors declare no conflicts of interests.

References

Achtert, P., & Tesche, M. (2014). Assessing lidar-based classification schemes for polar stratospheric clouds based on 16 years of measurements at Esrange, Sweden. *Journal of Geophysical: Research*, 119, 1386–1405. https://doi.org/10.1002/2013JD020355

Bi, L., Yang, P., Kattawar, G. W., & Mishchenko, M. I. (2013). Efficient implementation of the invariant imbedding T-matrix method and the separation of variables method applied to large nonspherical inhomogeneous particles. *J. Quant. Spectrosc. Ra.*, 116, 169–183.

Biermann, U. M. (1998), Gefrier- und FTIR-Experimente zur Nukleation und Lebensdauer stratosphärischer Wolken, PhD thesis, Universität Bielefeld, cuvillier Verlag, ISBN 3-89712-212-X

Biermann, U. M., Luo, B. P., & Peter, T. (2000). Absorption spectra and optical constants of binary and ternary solutions of H_2SO_4, HNO_3, and H_2O in the mid infrared at atmospheric temperatures. *The Journal of Physical Chemistry. A*, 104, 783–793.

Brooks, S. D., Baumgardner, D., Gandrud, B., Dye, J. E., Northway, M. J., Fahey, D. W., et al. (2003). Measurements of large stratospheric particles in the Arctic polar vortex. *Journal of Geophysical Research*, 108, 4652. https://doi.org/10.1029/2002JD003278

Carslaw, K. S., Kettleborough, J. A., Northway, M. J., Davies, S., Gao, R., Fahey, D. W., et al. (2002). A vortex-scale simulation of the growth and sedimentation of large nitric acid hydrate particles. *Journal of Geophysical Research*, 107, 8300. https://doi.org/10.1029/2001JD000467

Engel, I., Luo, B. P., Pitts, M. C., Poole, L. R., Hoyle, C. R., Grooß, J.-U., et al. (2013). Heterogeneous formation of polar stratospheric clouds —Part 2: Nucleation of ice on synoptic scales. *Atmospheric Chemistry and Physics*, 13, 10,769–10,785. https://doi.org/10.5194/acp-13-10769-2013

Fahey, D. W., Gao, R. S., Carslaw, K. S., Kettleborough, J., Popp, P. J., Northway, M. J., et al. (2001). The detection of large HNO_3-containing particles in the winter Arctic stratosphere. *Science*, 291(5506), 1026–1031. https://doi.org/10.1126/science.1057265

Fahey, D. W., Kelly, K. K., Kawa, S. R., Tuck, A. F., Loewenstein, M., Chan, K. R., & Heid, L. E. (1990). Observations of denitrification and dehydration in the winter polar stratosphere. *Nature*, 344, 321–324.

Fischer, H., Birk, M., Blom, C., Carli, B., Carlotti, M., von Clarmann, T., et al. (2008). MIPAS: An instrument for atmospheric and climate research. *Atmospheric Chemistry and Physics*, 8, 2151–2188. https://doi.org/10.5194/acp-8-2151-2008

Grooß, J.-U., Engel, I., Borrmann, S., Frey, W., Günther, G., Hoyle, C. R., Kivi, R., et al. (2014). Nitric acid trihydrate nucleation and denitrification in the Arctic stratosphere. *Atmospheric Chemistry and Physics*, 14, 1055–1073, https://doi.org/10.5194/acp-14-1055-2014

Grooß, J.-U., Günther, G., Müller, R., Konopka, P., Bausch, S., Schlager, H., et al. (2005). Simulation of denitrification and ozone loss for the Arctic winter 2002/2003. *Atmospheric Chemistry and Physics*, 5, 1437–1448. https://doi.org/10.5194/acp-5-1437-2005

Grothe, H., Tizek, H., Waller, D., & Stokes, D. J. (2006). The crystallization kinetics and morphology of nitric acid trihydrate. *Physical Chemistry Chemical Physics*, 8(19), 2232–2239. https://doi.org/10.1039/B601514J

Hanson, D., & Mauersberger, K. (1988). Laboratory studies of the nitric acid trihydrate: Implications for the south polar stratosphere. *Geophysical Research Letters*, 15, 855–858. https://doi.org/10.1029/GL015i008p00855

Höpfner, M., Luo, B. P., Massoli, P., Cairo, F., Spang, R., Snels, M., et al. (2006). Spectroscopic evidence for NAT, STS, and ice in MIPAS infrared limb emission measurements of polar stratospheric clouds. *Atmospheric Chemistry and Physics*, 6, 1201–1219. https://doi.org/10.5194/acp-6-1201-2006

Hoyle, C. R., Engel, I., Luo, B. P., Pitts, M. C., Poole, L. R., Grooß, J.-U., & Peter, T. (2013). Heterogeneous formation of polar stratospheric clouds—Part 1: Nucleation of nitric acid trihydrate (NAT). *Atmospheric Chemistry and Physics*, 13, 9577–9595. https://doi.org/10.5194/acp-13-9577-2013

Khosrawi, F., Kirner, O., Sinnhuber, B.-M., Johansson, S., Höpfner, M., Santee, M. L., et al. (2017). Denitrification, dehydration and ozone loss during the 2015/2016 Arctic winter. *Atmospheric Chemistry and Physics*, 17, 12,893–12,910. https://doi.org/10.5194/acp-17-12893-2017

Khosrawi, F., Urban, J., Pitts, M. C., Voelger, P., Achtert, P., Kaphlanov, M., et al. (2011). Denitrification and polar stratospheric cloud formation during the Arctic winter 2009/2010. *Atmospheric Chemistry and Physics*, 11, 8471–8487. https://doi.org/10.5194/acp-11-8471-2011

Kuttippurath, J., Godin-Beekmann, S., Lefèvre, F., Nikulin, G., Santee, M. L., & Froidevaux, L. (2012). Record-breaking ozone loss in the Arctic winter 2010/2011: Comparison with 1996/1997. *Atmospheric Chemistry and Physics*, 12, 7073–7085. https://doi.org/10.5194/acp-12-7073-2012

Livesey, N. J., Read, W. G., Wagner, P. A., Froidevaux, L., Lambert, A., Manney, G. L., et al. (2018). Version 4.2x Level 2 data quality and description document. Tech. Rep. JPL D-33509 Rev. D, Jet Propulsion Laboratory.

Manney, G. L., Santee, M. L., Froidevaux, L., Livesey, N. J., & Read, W. G. (2015). MLS/Aura L2 nitric acid (HNO_3) mixing ratio—Version 4.

Manney, G. L., Santee, M. L., Rex, M., Livesey, N. L., Pitts, M. C., Veefkind, P., et al. (2011). Unprecedented Arctic ozone loss in 2011. *Nature*, 478(7370), 469–475. https://doi.org/10.1038/nature10556

Molleker, S., Borrmann, S., Schlager, H., Luo, B., Frey, W., Klingebiel, M., Weigel, R., et al. (2014). Microphysical properties of synoptic-scale polar stratospheric clouds: In situ measurements of unexpectedly large HNO_3-containing particles in the Arctic vortex, *Atmospheric Chemistry and Physics*, 14, 10,785–10,801. https://doi.org/10.5194/acp-14-10785-2014

Murphy, D. M., & Koop, T. (2005). Review of the vapour pressures of ice and supercooled water for atmospheric applications. *Q. J. Roy. Meteor. Soc.*, 131, 1539–1565.

Northway, M. J., Gao, R. S., Popp, P. J., Holecek, J. C., Fahey, D. W., Carslaw, K. S., et al. (2002). An analysis of large HNO_3-containing particles sampled in the Arctic stratosphere during the winter of 1999/2000. *Journal of Geophysical Research-Atmospheres*, 107. SOL 41-1–SOL 41-22, https://doi.org/10.1029/2001JD001079

Peter, T. (1997). Microphysics and heterogeneous chemistry of polar stratospheric clouds. *Annual Review of Physical Chemistry*, 48, 785–822. https://doi.org/10.1146/annurev.physchem.48.1.785

Pitts, M. C., Poole, L. R., & Gonzalez, R. (2018). Polar stratospheric cloud climatology based on CALIPSO spaceborne lidar measurements from 2006 to 2017. *Atmospheric Chemistry and Physics*, 18, 10,881–10,913. https://doi.org/10.5194/acp-18-10881-2018

Poole, L. R., & McCormick, M. P. (1988). Polar stratospheric clouds and the Antarctic ozone hole. *Journal of Geophysical Research*, *93*, 8423–8430. https://doi.org/10.1029/JD093iD07p08423

Rex, M., Salawitch, R. J., Deckelmann, H., von der Gathen, P., Harris, N. R. P., Chipperfield, M. P., et al. (2006). Arctic winter 2005: Implications for stratospheric ozone loss and climate change. *Geophysical Research Letters*, *33*, L23808. https://doi.org/10.1029/2006GL026731

Rieder, H., & Polvani, L. M. (2013). Are recent Arctic ozone losses caused by increasing greenhouse gases? *Geophysical Research Letters*, *40*, 4437–4441.

Salawitch, R. J., Gobbi, G. P., Wofsy, S. C., & McElroy, M. B. (1989). Denitrification in the Antarctic stratosphere. *Nature*, *339*, 525–527.

Sinnhuber, B.-M., Stiller, G., Ruhnke, R., von Clarmann, T., Kellmann, S., & Aschmann, J. (2011). Arctic winter 2010/2011 at the brink of an ozone hole. *Geophysical Research Letters*, *38*. L24814 https://doi.org/10.1029/2011GL049784

Solomon, S. (1999). Stratospheric ozone depletion: A review of concepts and history. *Reviews of Geophysics*, *37*, 275–316. https://doi.org/10.1029/1999RG900008

Spang, R., & Remedios, J. J. (2003). Observations of a distinctive infrared spectral feature in the atmospheric spectra of polar stratospheric clouds measured by the CRISTA instrument. *Geophysical Research Letters*, *30*(16), D24211. https://doi.org/10.1029/2003GL017231

Spang, R., Remedios, J. J., & Barkley, M. P. (2004). Colour indices for the detection and differentiation of cloud types in infra-red limb emission spectra. *Advances in Space Research*, *33*, 1041–1047.

Stiller, G. P., von Clarmann, T., Funke, B., Glatthor, N., Hase, F., Höpfner, M., & Linden, A. (2002). Sensitivity of trace gas abundances retrievals from infrared limb emission spectra to simplifying approximations in radiative transfer modelling. *J. Quant. Spectrosc. Ra.*, *72*, 249–280. https://doi.org/10.1016/S0022-4073(01)00123-6

Tizek, H., Knözinger, E., & Grothe, H. (2004). Formation and phase distribution of nitric acid hydrates in the mole fraction range $xHNO_3 <$ 0.25: A combined XRD and IR study. *Physical Chemistry Chemical Physics*, *6*, 972–979. https://doi.org/10.1039/B310672A

Toon, O. B., Hamill, P., Turco, R. P., & Pinto, J. (1986). Condensation of HNO_3 and HCl in the winter polar stratospheres. *Geophysical Research Letters*, *13*(12), 1284–1287. https://doi.org/10.1029/GL013i012p01284

Toon, O. B., Turco, R. P., & Hamill, P. (1990). Denitrification mechanisms in the polar stratospheres. *Geophysical Research Letters*, *17*(4), 445–448. https://doi.org/10.1029/GL017i004p00445

Tritscher, I., Grooß, J.-U., Spang, R., Pitts, M. C., Poole, L. R., Müller, R., & Riese, M. (2019). Lagrangian simulation of ice particles and resulting dehydration in the polar winter stratosphere. *Atmospheric Chemistry and Physics*, *19*, 543–563. https://doi.org/10.5194/acp-19-543-2019

Voigt, C., Schreiner, J., Kohlmann, A., Zink, P., Mauersberger, K., Larsen, N., et al. (2000). Nitric acid trihydrate (NAT) in polar stratospheric clouds. *Science*, *290*(5497), 1756–1758. https://doi.org/10.1126/science.290.5497.1756

Waibel, A. E., Peter, T., Carslaw, K. S., Oelhaf, H., Wetzel, G., Crutzen, P. J., et al. (1999). Arctic ozone loss due to denitrification. *Science*, *283*(5410), 2064–2069. https://doi.org/10.1126/science.283.5410.2064

Waters, J. W., Froidevaux, L., Harwood, R. S., Jarnot, R. F., Pickett, H. M., Read, W. G., et al. (2006). The Earth observing system microwave limb sounder (EOS MLS) on the Aura satellite. *IEEE Transactions on Geoscience and Remote Sensing*, *44*, 1075–1092. https://doi.org/10.1109/TGRS.2006.873771

Weiss, F., Kubel, F., Galvez, O., Hoelzel, M., Parker, S. F., Baloh, P., et al. (2016). Metastable nitric acid trihydrate in ice clouds. *Angewandte Chemie, International Edition*, *55*(10), 3276–3280. https://doi.org/10.1002/anie.201510841

Westbrook, C. D. (2008). The fall speeds of sub-100 μm ice crystals. *Q. J. Roy. Meteor. Soc.*, *134*, 1243–1251.

WMO (World Meteorological Organization) (2018). Scientific assessment of ozone depletion: 2018, Global Ozone Research and Monitoring Project–Report No. 58, Chapter 4 by Langematz, U. and Tully, M. (Lead Authors), Calvo, N., Dameris, M., de Laat, A.T.J., Klekociuk, A., et al.: *Polar Stratospheric Ozone: Past, Present, and Future* (Chap. 4, pp. 4.1–4.63). World Meteorological Organization, Geneva, Switzerland.

Woiwode, W., Höpfner, M., Bi, L., Pitts, M. C., Poole, L. R., Oelhaf, H., et al. (2016). Spectroscopic evidence of large aspherical β-NAT particles involved in denitrification in the December 2011 Arctic stratosphere. *Atmospheric Chemistry and Physics*, *16*, 9505–9532. https://doi.org/10.5194/acp-16-9505-2016

Worsnop, D. R., Zahniser, M. S., Fox, L. E., & Wofsy, S. C. (1993). Vapor pressures of solid hydrates of nitric acid: Implications for polar stratospheric clouds. *Science*, *259*(5091), 71–74. https://doi.org/10.1126/science.259.5091.71

Zasetsky, A. Y., Khalizov, A. F., Earle, M. E., & Sloan, J. J. (2005). Frequency dependent complex refractive indices of supercooled liquid water and ice determined from aerosol extinction spectra. *The Journal of Physical Chemistry. A*, *109*(12), 2760–2764. https://doi.org/10.1021/jp044823c

Zhu, Y., Toon, O. B., Lambert, A., Kinnison, D. E., Bardeen, C., & Pitts, M. C. (2017). Development of a polar stratospheric cloud model within the Community Earth System Model: Assessment of 2010 Antarctic Winter. *Journal of Geophysical Research: Atmospheres*, *122*, 10,418–10,438. https://doi.org/10.1002/2017JD027003

Zhu, Y., Toon, O. B., Lambert, A., Kinnison, D. E., Brakebusch, M., Bardeen, C. G., et al. (2015). Development of a polar stratospheric cloud model within the Community Earth System Model using constraints on Type I PSCs from the 2010–2011 Arctic winter. *J. Adv. Model. Earth Sy.*, *7*, 551–585. https://doi.org/10.1002/2015MS000427

Zhu, Y., Toon, O. B., Pitts, M. C., Lambert, A., Bardeen, C., & Kinnison, D. E. (2017). Comparing simulated PSC optical properties with CALIPSO observations during the 2010 Antarctic winter. *Journal of Geophysical Research: Atmospheres*, *122*, 1175–1202. https://doi.org/10.1002/2016JD025191